



HAL
open science

Comparative Stability Study of a Dual Active Bridge-Based Battery Charger With Advanced Modulation Schemes

Martin Scohier, Olivier Deblecker, Bashir Bakhshideh Zad

► **To cite this version:**

Martin Scohier, Olivier Deblecker, Bashir Bakhshideh Zad. Comparative Stability Study of a Dual Active Bridge-Based Battery Charger With Advanced Modulation Schemes. The 26th European Conference on Power Electronics and Applications, GDR SEEDS France & EPE Association, Mar 2025, Paris, France. 10.34746/epe2025-0175 . hal-05107541

HAL Id: hal-05107541

<https://utc.hal.science/hal-05107541v1>

Submitted on 11 Jun 2025

HAL is a multi-disciplinary open access archive for the deposit and dissemination of scientific research documents, whether they are published or not. The documents may come from teaching and research institutions in France or abroad, or from public or private research centers.

L'archive ouverte pluridisciplinaire **HAL**, est destinée au dépôt et à la diffusion de documents scientifiques de niveau recherche, publiés ou non, émanant des établissements d'enseignement et de recherche français ou étrangers, des laboratoires publics ou privés.



Distributed under a Creative Commons Attribution 4.0 International License

Comparative Stability Study of a Dual Active Bridge-Based Battery Charger With Advanced Modulation Schemes

Martin Scohier, Olivier Deblecker, Bashir Bakhshideh Zad
Electrical Engineering Division, Engineering Faculty, University of Mons
31, Bd. Dolez
Mons, Belgium
Tel.: +3265374154
E-Mail: martin.sochier@umons.ac.be
URL: www.epeu-umons.be

Index Terms—Small-signal stability, Battery charger, Dual Active Bridge (DAB), Modulation scheme

Abstract—Thanks to their galvanic isolation and bidirectional power transfer features, the Dual Active Bridge (DAB) converters can offer a promising solution for interconnecting battery chargers to emerging DC grid applications. When cascaded with LC filters, the charger stability can be affected by the impedance interactions caused by the closed-loop charging process. This is exacerbated by the wide range of operating points in terms of DC voltages as well as the numerous Modulation Schemes (MS). To address this, the current paper extends the averaged small-signal model to the case of a Constant Current Constant Voltage (CC-CV) charging process. A stability analysis method is proposed to compare Single, Extended, Dual and Triple Phase Shift MS during a charging cycle. Simulation results validate the proposed models and highlight the flaws of advanced MS under varying operating conditions.

I. INTRODUCTION

Nowadays, the emerging of energy storage systems and the growing demand for Electric Vehicles (EV) are key drivers promoting research on battery system enhancement. Beside the rapid innovation in the field of battery technology and monitoring, advanced power electronics and control methods are required to safely manage the battery charge and discharge. Hence, battery chargers are power converters, often cascaded with filters and front-end converters that ultimately control the power at the battery ports, ensuring efficient and life-lasting operation. Conventional chargers use front-end AC-DC converters in AC grids but the growing adoption of DC grids allows to consider single stage DC-DC converter topologies [1]. With their medium frequency

transformer, Isolated Bidirectional DC-DC (IBDC) converters offer seamless voltage matching at high power density.

A versatile bidirectional battery charger configuration is presented in Figure 1 where LC filters are connected in cascade to an IBDC converter for switching harmonics rejection on both sides. However, such a power conversion chain is challenged by the inherent impedance interactions of each individual system. Indeed, The stability challenge of LC cascaded systems in DC grids is well-known and passive and active damping approaches are discussed in [2]. Those approaches however require the evaluation of the cascaded elements input and output impedances, that significantly depend on the operating point, the control and modulation schemes. In addition, the inherent variations in battery cell voltage, along with voltage disturbances on the DC grid side, call for consideration of significant DC voltage variations around the rated operating point.

The Dual Active Bridge (DAB) is an IBDC converter widely studied for its applications in solid state transformers, railway and aerospace onboard equipment. It allows for the conversion at high power density of a

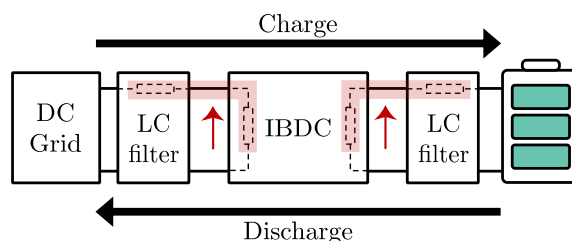


Fig. 1: Power conversion chain of a DC grid-tied battery charger.

wide range of input and output voltages thanks to its medium frequency transformer [3], making it a popular topology in battery systems especially in EV onboard and off-board chargers. Despite the ease of implementing Single Phase Shift (SPS) modulation for the power transfer control, higher losses occur as the input and output DC voltages depart from their rated values. To address this, advanced modulation techniques such as Extended Phase Shift (EPS), Dual Phase Shift (DPS) and Triple Phase Shift (TPS) [4] have been proposed in literature. These modulations utilize the inner duty cycles of the primary- and/or secondary-side AC voltages to shape the inductor current depending on the desired objective. Each of these modulation comes with operational boundaries. Therefore, in order to extend the operating range of the DAB converter, multiple modes are combined to form a holistic Modulation Scheme (MS) [5]–[7]. The stability challenge of LC-DAB systems is most often analyzed with regard to SPS modulation only [8], [9]. A two-stage Constant Current Constant Voltage (CC-CV) battery charger is considered in [10] but it emphasizes on the impedance shaping in the AC-DC converter. Concerning the DAB converter with advanced MS, modulator comparison and active damping strategy are proposed in [11], [12] but are limited to a restricted operating range. Moreover, the study in [13] develops comprehensive small-signal stability analysis able to decouple the modulator from the impedance of the converter. This however complicates the practical modulator implementation as it introduces an intermediate control variable.

To tackle this issue, a study highlighted the role of MS design in the stability of LC-DAB systems [14]. To that end, an averaged small-signal model, valid for advanced MS, was proposed. Nevertheless, the stability analysis was conducted with only one TPS MS on a resistive load. To address this limitation, the main contribution on this paper is to extend the models to a DAB-based battery charger. The closed-loop model of the input impedance is therefore developed, considering CC-CV charging in a wide range of voltage variations. Secondly, a stability analysis of a battery charging cycle is performed to compare the use of three advanced MS.

The remainder of the paper is organized as follows. Section II details the operation and the control of the DAB-based battery charger. Section III then extends the averaged small-signal models to a CC-CV charging process. Finally in Section IV, the stability analysis is performed over an entire charging cycle. It is shown that the models accurately expose the stability margin enhancement or degradation caused by an advanced MS.

II. DESCRIPTION OF THE DAB-BASED BATTERY CHARGER

The DAB-based battery charger circuit is shown in Figure 2. The battery, DAB converter and filters are represented along with the modulator and controller. For the DAB converter, v_d (i_d) and v_o (i_o) are the input and output voltages (currents), respectively. Their average values over one switching period T_s ($= 1/f_s$) are denoted as V_d , V_o , I_d , and I_o .

1) *DC grid side*: To represent a scenario that is both challenging and realistic, we consider a 1.5 kV railway DC grid, characterized by significant variations in average voltage, $\pm 33\%$ of the rated value, as well as frequent voltage spikes. The filter inductor L_f and its equivalent series resistor (ESR) R_f form with the converter input capacitor C_d the LC filter required for harmonic rejection and voltage spike protection. The resonant frequency is typically set to a few tens of Hertz.

2) *Battery side*: A Li-Ion EV battery pack with rated voltage and charging current of 700 V and 150 A is considered here. The battery is modeled with a constant open circuit (OC) voltage V_b in series with an impedance Z_b . The latter is the combination of the battery internal resistance R_b and the filtering inductor L_b that smooths out the battery current ripple. The OC voltage V_b is related to the State of Charge (SoC) of the battery following the model in [15]. Figure 3 shows the evolution of the electrical characteristics of the battery during a common CC-CV charging process.

First, V_b rises from 500 to 770 V while charged at a constant current of 150 A. Also, the output voltage of the converter V_o rises along V_b to compensate the voltage drop on R_b . When $V_b = V_b^{cv}$ (770 V), V_o reaches the maximum voltage and is thus fixed as a reference. The

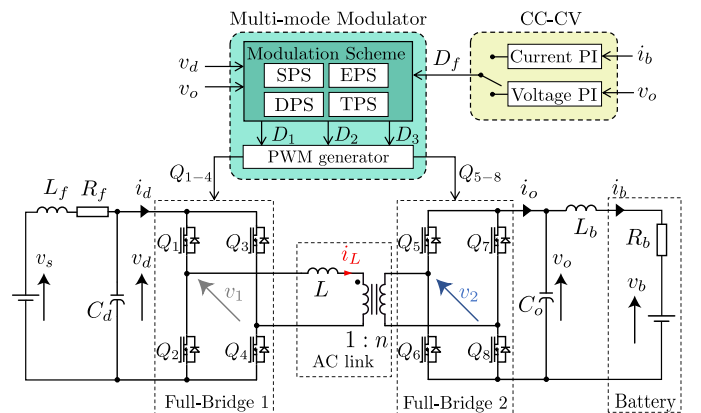


Fig. 2: Power converter and control diagram of the DAB-based battery charger.

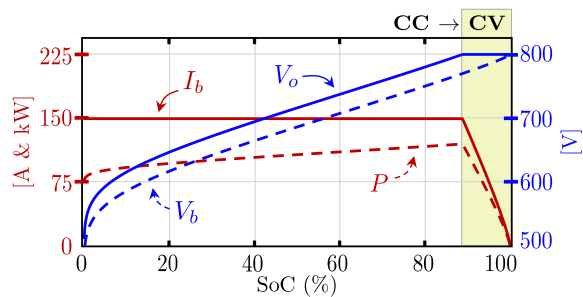


Fig. 3: Electrical characteristics of the battery pack with a CC-CV charging process.

charging current and power then slowly decrease until the battery is fully charged (i.e. when $V_b = V_b^{max}$). The CC-CV charging process is implemented as two controllers with fixed parameters throughout the entire operating range for current and voltage regulation.

3) *DAB converter with advanced MS*: As indicated above, voltage variations from the DC grid and battery sides will significantly alter the operation of the DAB converter. For convenience, we define the voltage ratio as

$$d = \frac{V_o}{nV_d} \quad (1)$$

The current in the AC power inductor i_L is controlled by the two-level square wave AC voltages v_1 and v_2 . The resulting average power P is considered positive during the battery charging. Hence, the converter operates in *boost* mode when d is greater than one (i.e. $V_d < V_o/n$). Inversely, *buck* mode stands for values of $d < 1$. In conventional designs, the transformer turns ratio n is chosen to ensure $d \approx 1$ at rated conditions. Thereafter, the normalized power is given by

$$P_n = P \frac{8nf_s L}{V_d V_o} \quad (2)$$

Assuming a fixed switching frequency, the adequate switching of the transistors Q_{1-8} adjusts the amplitude and phase of v_1 and v_2 . The inner duty cycles D_1 and D_2 , and the phase-shift ratio D_3 are the three control variables used to generate the gate pulse signals (see Figure 4). An infinite number of control variable combinations exist for the same operating point (OP). A modulation scheme is therefore defined here as set of functions that maps an operating point (d, P_n) to a control variable combination (D_1, D_2, D_3) . Numerous MS are derived in literature and differ from their optimization objectives (e.g. conduction, switching or total losses minimization). While TPS modulation generally defines the use of the three control variables, the SPS, EPS

TABLE I: Selected Modulation Schemes.

Advanced MS	Minimization objective	Number of Modes
EPS [6]	Conduction losses	5 { Low P (<i>buck, boost</i>) High P (<i>buck, boost</i>) SPS
DPS [5]	Peak inductor current	4 { Low P (<i>buck, boost</i>) High P (<i>buck, boost</i>)
TPS [7]	Backflow power	4 { Low P (<i>buck, boost</i>) High P (<i>buck, boost</i>)

and DPS appellations refer to sub-categories respectively defined as $(D_1 \wedge D_2 = 1)$, $(D_1 \vee D_2 = 1)$, and $(D_1 = D_2)$. In addition to SPS, three advanced MS are selected in literature based on their high performances with low complexity. As shown in Table I, a small amount of modes is preferred where the control variables calculation is simple and unified between each mode. To that end, we use the fundamental phase shift angle between v_1 and v_2 as a unified variable to control the transferred power. It is expressed as

$$D_f = D_3 + \frac{D_2}{2} - \frac{D_1}{2} \quad (3)$$

For each selected mode, the operating range as well as the unified control variable to transferred power function are found in Appendix, Table III. Moreover, the tables mapping D_f into (D_1, D_2, D_3) can be found in the respective papers. Figure 4 displays an example of AC voltages and inductor current waveforms using the selected MS at identical operating conditions (Low power in *boost* mode).

Then, for illustration purposes, Figure 5 depicts the range of normalized operating points of the modes that constitute the four selected MS. While SPS operates uniformly across the entire range (see Figure 5a), different modes are employed depending on the power level with the advanced MS. On top of that, dashed arrows represent the trajectory of operating points during the charging process, distinguishing between low and high supply voltage conditions. This highlights the multimodal operation of the DAB-based battery charger with advanced MS.

Finally, the specifications of the studied system are found in Table II. The converter parameters are taken from the previous design of a DAB converter for a DC railway auxiliary power supply that operates in similar input and output ranges (see [16], [17]).

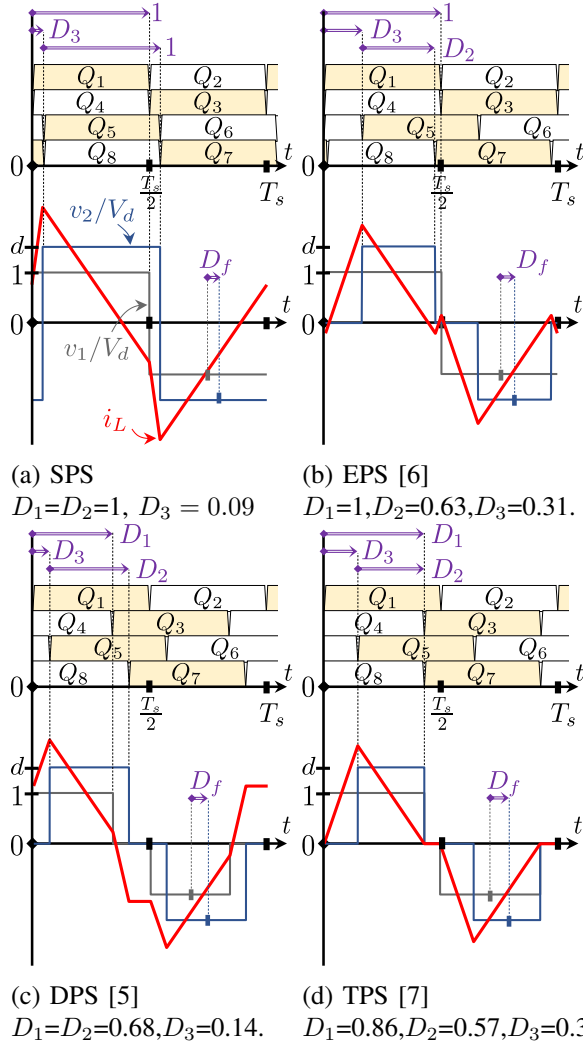


Fig. 4: AC link waveform and switching signals at $P_n = 1/3$ and $d = 3/2$ (Low P , boost mode).

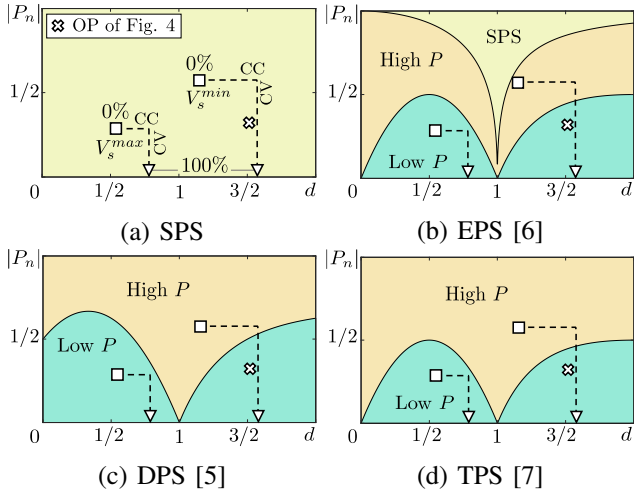


Fig. 5: Normalized operating range of the selected MS.

TABLE II: Specifications of the considered system.

	Symbol	Value
Rated supply voltage	V_s	1 ~ 2 kV
Filter inductance	L_f	4 mH
Filter ESR	R_f	300 m Ω
Input Capacitor	C_d	1 mF
Output capacitor	C_o	1 mF
Output filter inductance	L_b	5 μ H
Battery internal resistance	R_b	200 m Ω
Battery OC voltage range	V_b	500 ~ 800 V
Battery rated charging current	I_b^{max}	150 A
Rated Power	P^{max}	120 kW
Switching frequency	f_s	5 kHz
Transformer turns ratio	n	21/41
AC inductance	L	187.5 μ H
Current controller parameters	k_v, T_v	0.001, 5 ms
Voltage controller parameters	k_i, T_i	0.005, 5 ms

III. SMALL-SIGNAL MODEL

Because the multi-mode modulator serves as the intermediate between the controller and the DAB converter, different dynamics are to be observed between the different MS. A linear approach for controller design is preferred as it allows for well established stability analysis. Therefore, small-signal linearization and PI controllers are used. The averaged small-signal model of the DAB converter, presented in [14], is valid for the studied MS given in Table I. It assumes that the DAB converter is made out of two current sources by neglecting the high-order dynamics in the AC link. Next, the input and output currents are averaged over one switching period and are equal to $I_d = P/V_d$ and $I_o = P/V_o$, by assuming no losses in the converter. The large-signal current sources are therefore expressed as

$$\begin{cases} I_d = \frac{1}{8nf_sL} \cdot V_o \cdot P_n(D_f, V_d, V_o) \\ I_o = \frac{1}{8nf_sL} \cdot V_d \cdot P_n(D_f, V_d, V_o) \end{cases} \quad (4)$$

where $P_n(D_f, V_d, V_o)$ for each mode is obtained in Table III. By applying small-signal perturbations $\tilde{d}_f, \tilde{v}_d, \tilde{v}_o$ to (4) around an equilibrium point (D_f, V_d, V_o) , the small-signal current sources can be expressed as a product of matrix

$$\begin{pmatrix} \tilde{i}_d \\ \tilde{i}_o \end{pmatrix} = \begin{pmatrix} G_{i_d d_f} & G_{i_d v_d} & G_{i_d v_o} \\ G_{i_o d_f} & G_{i_o v_d} & G_{i_o v_o} \end{pmatrix} \begin{pmatrix} \tilde{d}_f \\ \tilde{v}_d \\ \tilde{v}_o \end{pmatrix} = G_{ij} \begin{pmatrix} \tilde{d}_f \\ \tilde{v}_d \\ \tilde{v}_o \end{pmatrix} \quad (5)$$

where G_{ij} , the matrix of small-signal current gains, is the Jacobian matrix of the function in (4) expressed as

$$G_{ij} = \frac{1}{8n_f s L} \cdot \begin{pmatrix} \frac{\partial(V_o \cdot P_n)}{\partial D_f} & \frac{\partial(V_o \cdot P_n)}{\partial V_d} & \frac{\partial(V_o \cdot P_n)}{\partial V_o} \\ \frac{\partial(V_d \cdot P_n)}{\partial D_f} & \frac{\partial(V_d \cdot P_n)}{\partial V_d} & \frac{\partial(V_d \cdot P_n)}{\partial V_o} \end{pmatrix} \quad (6)$$

The equivalent small-signal circuit of the battery charger is shown in Figure 6 where the grid and battery sides are represented as their Thevenin equivalent voltage sources $\tilde{v}_{td}, \tilde{v}_{to}$ and impedances Z_f, Z_o defined as

$$Z_f(s) = \frac{sL_f + R_f}{s^2 L_f C_d + sR_f C_d + 1} \quad (7)$$

$$Z_o(s) = \frac{Z_b}{sC_o Z_b + 1} \quad (8)$$

with the battery impedance equal to $Z_b(s) = R_b + sL_b$. Finally, the open-loop model is completed by the following equations

$$\tilde{v}_d = \tilde{v}_{td} - Z_f \tilde{i}_d \quad (9)$$

$$\tilde{v}_o = \tilde{v}_{to} + Z_o \tilde{i}_o \quad (10)$$

$$\tilde{i}_b = \tilde{v}_o / Z_b \quad (11)$$

The diagram of the control structure is shown in Figure 7. It includes the open-loop model and the control structure of the CC-CV charging.

Depending on the charging state, the controller outputs the unified control variable, defined as

$$\tilde{d}_f = \begin{cases} C_i(\tilde{i}_b^* - \tilde{i}_b) & , CC \\ C_v(\tilde{v}_o^* - \tilde{v}_o) & , CV \end{cases} \quad (12)$$

with $C_i(s) = k_i(1 + 1/sT_i)$ and $C_v(s) = k_v(1 + 1/sT_v)$, two PI controllers responsible of the constant current

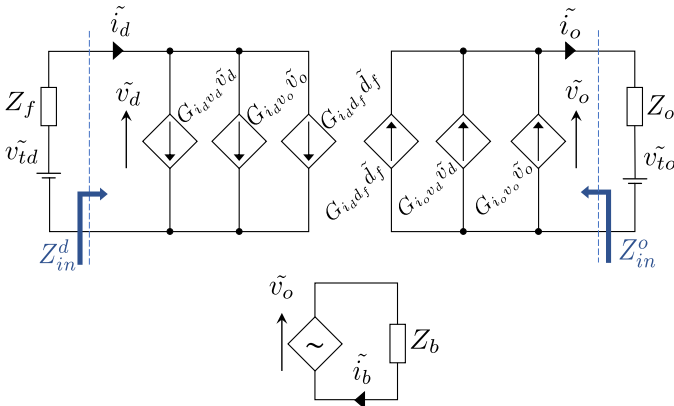


Fig. 6: Averaged small-signal model of the battery charger.

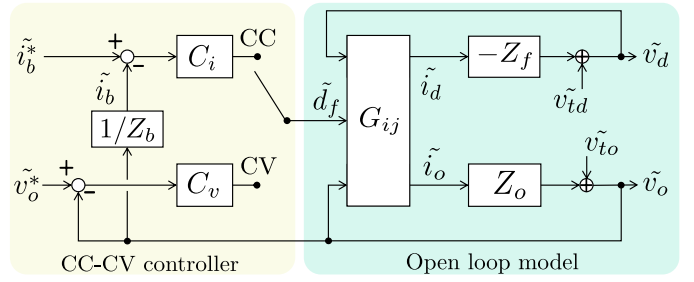


Fig. 7: Block diagram of the CC-CV charger control.

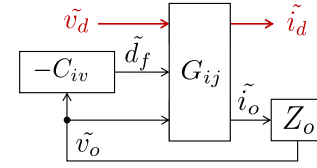


Fig. 8: Simplified diagram for the calculation of Z_{in}^d .

and constant voltage regulation, respectively. Here, the reference terms $\tilde{v}_o^*, \tilde{i}_b^*$ and the voltage perturbations $\tilde{v}_{td}, \tilde{v}_{to}$ are set to zero. By rearranging the controllers as in eq. (13), a simplified diagram can be drawn in Figure 8 for the calculation of the input impedance.

$$C_{iv} = \begin{cases} C_i/Z_b & , CC \\ C_v & , CV \end{cases} \quad (13)$$

Hence, by combining eqs. (5), (9), (10) and (12), the input impedance is calculated as follows :

$$Z_{in}^d = \left(\frac{\tilde{i}_d}{\tilde{v}_d} \right)^{-1} = \left(\frac{Z_o G_{i_o v_d} (G_{i_d v_o} - G_{i_d d_f} C_{i_o})}{1 - Z_o (G_{i_o v_o} - G_{i_o d_f} C_{i_v})} + G_{i_d v_d} \right)^{-1} \quad (14)$$

Now, the interacting impedances can be fully derived for any operating point, modulation scheme, filter and controller parameters.

A. Stability criterion

At the DC grid side of the converter (see Figure 6), the input voltage resulting from the impedance interaction is expressed as

$$\tilde{v}_d = \frac{1}{1 + Z_f/Z_{in}^d} \tilde{v}_{td} \quad (15)$$

From Eq. (15), the Nyquist stability criterion states that the impedance ratio Z_f/Z_{in}^d should not encircle the (0 dB, 180°) critical point. Both the Phase Margin (PM)

and Gain margin (GM), defined in Eq. (16), must be positive for small-signal stability [2]. We define each margin as follows

$$\begin{cases} GM(dB) = |Z_{in}^d(j2\pi f_p)| - |Z_f(j2\pi f_p)| > 0 \\ PM(^{\circ}) = 180^{\circ} + \angle Z_{in}^d(j2\pi f_g) - \angle Z_f(j2\pi f_g) > 0 \end{cases} \quad (16)$$

where f_g and f_p , are the crossing frequencies.

Regarding the battery side, the stability criterion is analogous to that described but with the ratio Z_o/Z_{in}^o . This is however not addressed in this paper.

B. Model validation on studied system

For validation purposes, the DAB-based battery charger and control structure are implemented on a switching model in PLECS. An operating point at maximum charging power is simulated at low and high V_s . Once steady-state is reached, a small multitone signal is added to v_d while the harmonic response of i_d is observed. The Bode diagram of the interacting impedances and the Black diagram of the impedance ratio are displayed in Figure 9. The linear modeling of Z_{in}^d is depicted using continuous lines, while the harmonic response of the switched model is represented by discrete markers. One can note that the developed models match the switched model with high accuracy within this frequency range.

Furthermore, it can be observed that the input impedance is independent of the MS at low frequencies while it greatly differs above 10 Hz. In this case where the resonant frequency is of the same order of magnitude than the controller bandwidth, the stability will be significantly impacted by the MS. Concerning the Black diagram, because the critical point is never encircled, the charger is stable for all presented cases. Regarding stability margins, the PM is always infinite as the 0 dB axis is never crossed. Still, the GM, measured by the distance between the critical point and the crossing of the 180° axis, depends on the supply voltage as well as the selected MS. Under low supply voltage condition (i.e. in *boost* mode), the advanced modulation schemes result in a higher GM than for SPS. However, in *buck* mode, the opposite is observed where DPS and TPS modulation almost lead to instability.

IV. STABILITY ANALYSIS OF A CHARGING CYCLE

This section provides a stability analysis during one complete charging cycle. The stability at the input side is analyzed for each operating point of the CC-CV charging under high and low supply voltage conditions following the flowchart shown in Figure 10. First, the equilibrium state values are calculated according to the SoC (see

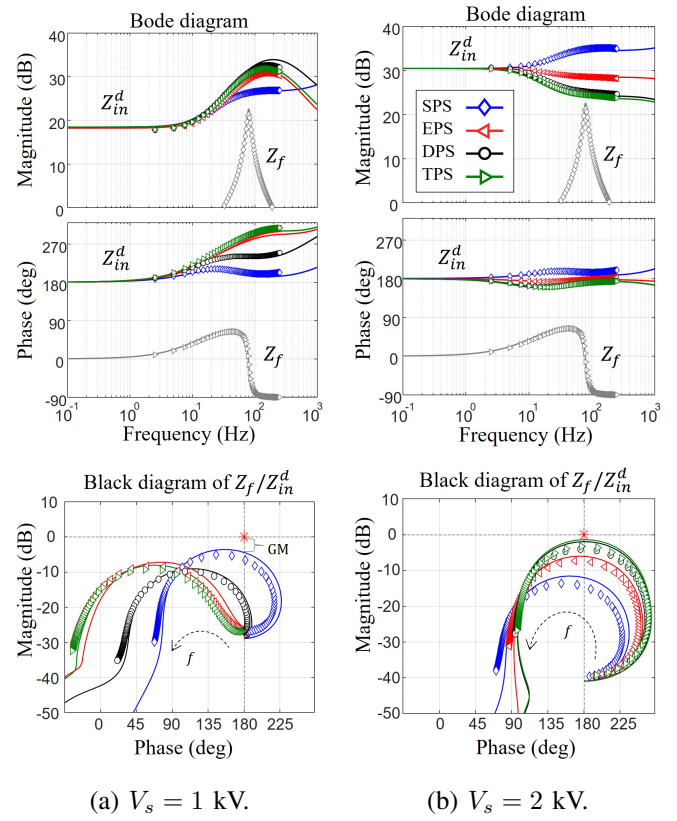


Fig. 9: Bode and Black diagrams of Z_f , Z_{in}^d and their ratio at P^{max} .

Figure 3). Then, the small-signal model is obtained for each MS. Finally, the input impedance is calculated by mean of (14), enabling the stability margin evaluation.

Figure 11 shows the modeled GM during the charging process for each MS under low and high supply voltage conditions. We first notice that the CV mode shows no concern due to the reduced transferred power. In Figure 11a, the use of an advanced MS increases the GM in comparison with SPS. However, Figure 11b shows a significant stability margin degradation when using EPS, DPS and TPS MS. This indicates that in *buck* mode, the advanced modulations have a negative impact on the system stability.

In order to compare with those observations, a 1ms, 100 V pulse is generated as a disturbance on the supply voltage of the PLECS model. The responses of v_d , i_o and i_L are observed in Figure 12. It can be seen from the oscillations of v_d that SPS exhibits a quicker recovery after the disturbance. Inversely, as predicted by the linear models, DPS and TPS show a slow recovery which translates into a reduced stability margin. Finally, it must be reminded that advanced MS are mainly used to minimize the power losses. Despite the fluctuating results

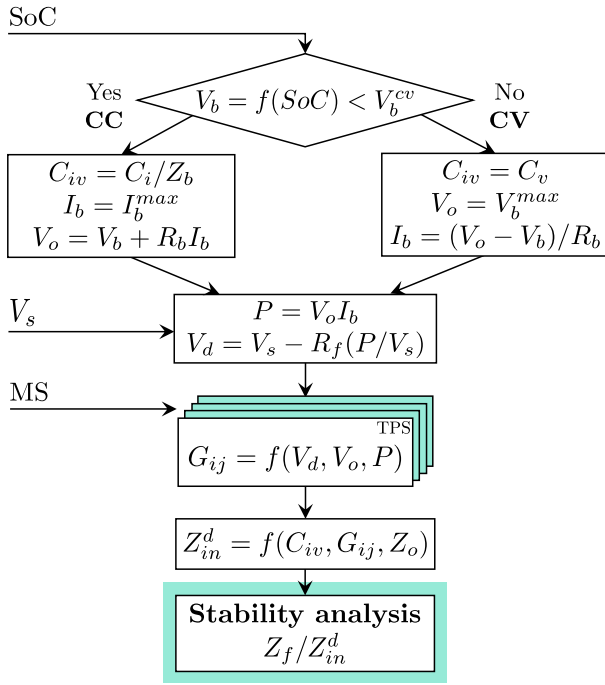
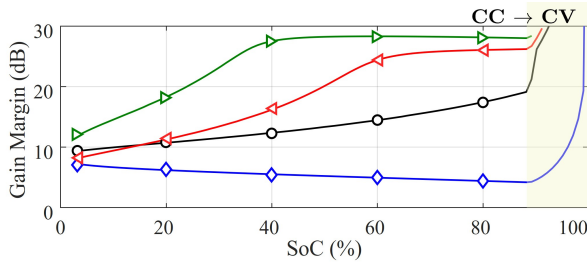
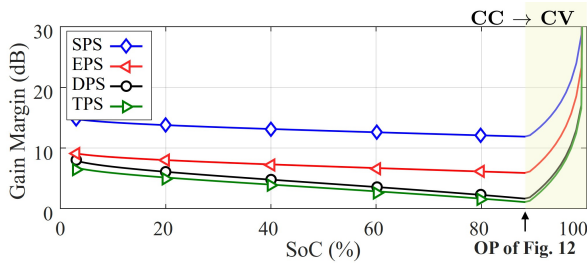


Fig. 10: Flowchart of the stability analysis over the charging cycle.



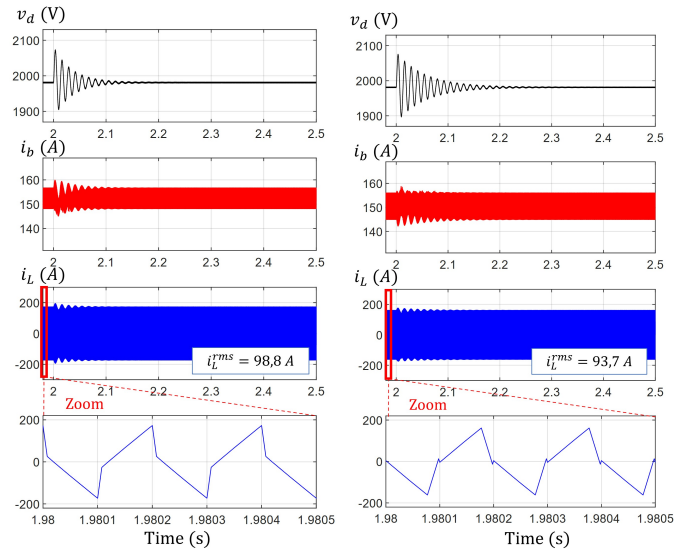
(a) $V_s = 1$ kV (*boost mode*)



(b) $V_s = 2$ kV (*buck mode*)

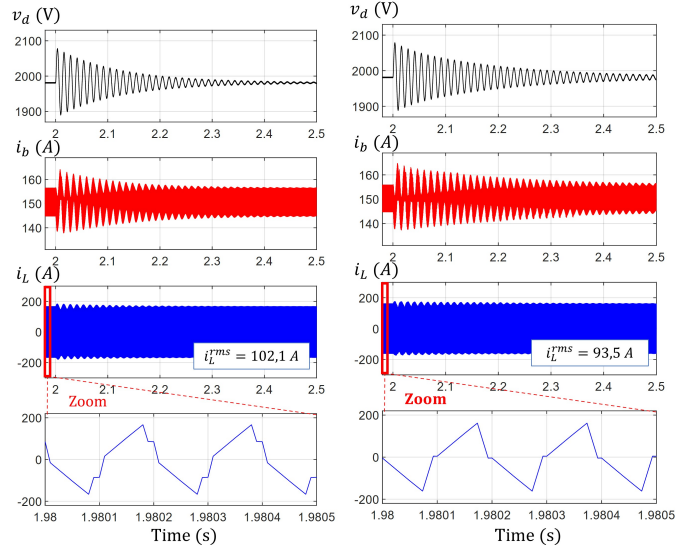
Fig. 11: Modeled GM as a function of the SoC and MS.

with regard to stability, EPS and TPS are expected to reach higher efficiency as indicated by their lower RMS inductor current. This confirms that a comprehensive stability analysis is required for MS selection.



(a) SPS

(b) EPS



(c) DPS

(d) TPS

Fig. 12: Supply voltage pulse response at P^{max} , $V_s = 2$ kV (*buck mode*).

V. CONCLUSION

In this work, the averaged small-signal model of a DAB-based charger with a CC-CV charging process is proposed. It is shown that despite their optimized performances in steady-state, the advanced MS have a large impact on the converter input impedance. The models are validated by simulation and a method for stability margin evaluation is proposed for each operating point of a charging cycle, highlighting the poor dynamic response of advanced MS in *buck mode*. Finally this work enables the comprehensive design of the modulator,

controllers and filters in order to achieve safe and efficient battery charging. Further research will explore the non-linearity of the advanced MS for increased accuracy. Nonetheless, the impedance interactions in the case of multiple parallel chargers will be considered.

APPENDIX

TABLE III: Operating range and transferred power function of the selected modes.

Mode	Operating Range	$ P_n = f(\delta^I, D_f)$
SPS	$\forall(\delta, P_n)$	$4 D_f (1 - D_f)$
EPS Low P	$ P_n \in [0, 2\delta(1 - \delta)[$	$\frac{4\delta}{(2-\delta)} D_f (1 + 2 D_f)$
EPS High P	$ P_n \in \left[2\delta(1 - \delta), 1 - \left(\frac{\sqrt{1-\delta^2}-1}{\delta} \right)^2 \right[$	$4 D_f (1 - D_f) - (1 - D_\alpha^{II})^2$
DPS Low P	$ P_n \in \left[0, \frac{1+2\delta-3\delta^2}{2} \right[$	$\frac{1+3\delta}{1-\delta} 2 D_f ^2$
DPS High P	$ P_n \in \left[\frac{1+2\delta-3\delta^2}{2}, 1 \right]$	$1 - \frac{3\delta^2-2\delta+1}{2\delta^2} (1 - 2 D_f)^2$
TPS Low P	$ P_n \in [0, 2\delta(1 - \delta)[$	$\frac{8\delta}{1-\delta} D_f ^2$
TPS High P	$ P_n \in [2\delta(1 - \delta), 1]$	$1 - \frac{2\delta^2-2\delta+1}{\delta^2} (1 - 2 D_f)^2$

^I $\delta = d^{sgn(1-d)}$ is used to handle *buck* and *boost* modes in a unified manner.

^{II} D_α is a control variable used in the EPS MS (see [6]).

REFERENCES

- [1] M. Berrehil El Kattel, R. Mayer, F. Ely, and B. de Jesus Cardoso Filho, "Comprehensive review of battery charger structures of EVs and HEVs for levels 1–3," *International Journal of Circuit Theory and Applications*, vol. 51, DOI 10.1002/cta.3579, no. 7, pp. 3514–3542, 7 2023.
- [2] R. Kumar and C. N. Bhende, "Active Damping Stabilization Techniques for Cascaded Systems in DC Microgrids: A Comprehensive Review," 2 2023.
- [3] F. Krismer, "Modeling and optimization of bidirectional dual active bridge DC-DC converter topologies," Ph.D. dissertation, ETH Zurich, Zürich, 2010.
- [4] N. Hou and Y. W. Li, "Overview and Comparison of Modulation and Control Strategies for a Nonresonant Single-Phase Dual-Active-Bridge DC-DC Converter," *IEEE Transactions on Power Electronics*, vol. 35, DOI 10.1109/TPEL.2019.2927930, no. 3, pp. 3148–3172, 2020.
- [5] M. Kim, M. Rosekeit, S. K. Sul, and R. W. De Doncker, "A dual-phase-shift control strategy for dual-active-bridge DC-DC converter in wide voltage range," *8th International Conference on Power Electronics - ECCE Asia: "Green World with Power Electronics"*, ICPE 2011-ECCE Asia, DOI 10.1109/ICPE.2011.5944548, pp. 364–371, 2011.
- [6] B. Liu, P. Davari, and F. Blaabjerg, "An Optimized Hybrid Modulation Scheme for Reducing Conduction Losses in Dual Active Bridge Converters," *IEEE Journal of Emerging and Selected Topics in Power Electronics*, vol. 9, DOI 10.1109/JESTPE.2019.2956323, no. 1, pp. 921–936, 2 2021.
- [7] S. Shao, M. Jiang, W. Ye, Y. Li, J. Zhang, and K. Sheng, "Optimal Phase-Shift Control to Minimize Reactive Power for a Dual Active Bridge DC-DC Converter," *IEEE Transactions on Power Electronics*, vol. 34, DOI 10.1109/TPEL.2018.2890292, no. 10, pp. 10 193–10 205, 2019.
- [8] F. Lin, X. Zhang, and F. Feng, "Modeling and Stability Analysis of the Cascaded Dual Active Bridge Converter System with Considerations of the Controller Parameters," in *2019 10th International Conference on Power Electronics and ECCE Asia (ICPE 2019 - ECCE Asia)*, DOI 10.23919/ICPE2019-ECCEAsia42246.2019.8796930, pp. 1817–1820, 2019.
- [9] Y. Eto, Y. Noge, M. Shoyama, and T. Babasaki, "Stability Analysis of Bidirectional Dual Active Bridge Converter With Input and Output LC Filters Applying Power-Feedback Control," *IEEE Transactions on Power Electronics*, vol. 38, DOI 10.1109/TPEL.2022.3225113, no. 3, pp. 3127–3139, 2023.
- [10] V. M. Iyer, S. Gulur, and S. Bhattacharya, "Small-signal stability assessment and active stabilization of a bidirectional battery charger," *IEEE Transactions on Industry Applications*, vol. 55, DOI 10.1109/TIA.2018.2871101, no. 1, pp. 563–574, 2019.
- [11] F. Feng, H. B. Gooi, and U. Manandhar, "Comparison of SPS, DPS and CTPS Modulations with Full Consideration of Stability of DAB Converters with Input LC Filter," in *Proceedings of the Energy Conversion Congress and Exposition - Asia, ECCE Asia 2021*, DOI 10.1109/ECCE-Asia49820.2021.9478977, pp. 98–103. Institute of Electrical and Electronics Engineers Inc., 5 2021.
- [12] F. Feng, X. Zhang, F. Lin, and H. B. Gooi, "Stability Analysis and Optimization of Dual Active Bridge Converter with LC Input Filter," in *2019 IEEE International Conference on Industrial Technology (ICIT)*, DOI 10.1109/ICIT.2019.8754992, pp. 544–549, 2019.
- [13] Y. Chen, Y. Zhang, E. Qu, and M. He, "Active Damping Method for LC-DAB System Based on a Power-Based Impedance Model," *IEEE Transactions on Power Electronics*, vol. 38, DOI 10.1109/TPEL.2022.3230218, no. 4, pp. 4405–4418, 4 2023.
- [14] M. Scohier, M. L. Gajardo, O. Deblecker, and T. Dragičević, "An Informed Modulation Strategy for Stability Enhancement of Dual Active Bridge Converters under Varying Supply Conditions," DOI 10.36227/tehrxiv.173747676.69845353/v1, 1 2025.
- [15] C. Zhang, J. Jiang, L. Zhang, S. Liu, L. Wang, and P. C. Loh, "A generalized SOC-OCV model for lithium-ion batteries and the SOC estimation for LNMCO battery," *Energies*, vol. 9, DOI 10.3390/en9110900, no. 11, 11 2016.
- [16] M. Scohier, O. Deblecker, and C. Valderrama, "Triple-Phase-Shift Controlled Dual Active Bridge Converter with Variable Input Voltage in Auxiliary Railway Supply," *24th European Conference on Power Electronics and Applications (EPE'22 ECCE Europe)*, Hanover, Germany, pp. 1–10, 2022.
- [17] M. Scohier, O. Deblecker, and B. Bakhshideh Zad, "A Simple and Effective Active Damping Method for Triple-Phase-Shift DAB Converter in DC Railway," in *IECON 2023- 49th Annual Conference of the IEEE Industrial Electronics Society*, DOI 10.1109/IECON51785.2023.10312325, pp. 1–6, 2023.